Droop coefficient placements for grid-side energy storage considering nodal frequency constraints under large disturbances

Jiawei Zhang [a], Jiaxin Wang [a], Ning Zhang [a,*], Peng Wang [a], Yating Wang [b], Chen Fang [c]

[a] *Department of Electrical Engineering, Tsinghua University, Beijing 100084, China*
[b] *China Electric Power Planning and Engineering Institute, Beijing 100120, China*
[c] *State Grid Shanghai Municipal Electric Power Company, Shanghai 200122, China*

ARTICLE INFO

ABSTRACT

The high-voltage cross-regional power injections threaten the power systems under high renewable penetrations. The system operators should keep the frequency nadirs within restrictions after possible large disturbances to guarantee frequency stability. However, the heterogeneous characteristics, including the network topology, differences in disturbance locations, regulation units, and operating modes, make the nodal frequency response behaviors different after large disturbances. Therefore, the center of inertia frequency is unsuitable for evaluating the frequency stability of the entire power system. At the same time, the primary regulations from energy storage with proper droop settings are expected to solve the power grid's frequency stability problems. This paper focuses on the droop coefficient placements for grid-side energy storage, considering nodal frequency constraints. We use data-driven methods, i.e., alternative support vector machine trees (ASVMTREE), to extract the rules of different droop placement strategies' influences on nodal frequency stability. Then, We optimize the droop coefficient of grid-side energy storage for typical operating modes. Finally, we verify the method on modified IEEE 39 and 118-bus test systems to show its effectiveness.

1. Introduction

The frequency stability under high renewable penetrations is a critical problem for modern power systems due to the low inertia and primary regulation resources [1]. In China, more than 20 cross-regional high-voltage transmission systems carry three to four gigawatts (GW) power injections each to the receiver grids [2,3]. They bring green energy from inland to China's coastal provinces, as shown in Fig. 1. Nevertheless, their occasional commutation failures become the largest threat to frequency stability, especially on the receiver power systems.

The large disturbances may bring drastic frequency drops near the access points in receiver power grids. The nodal frequencies are various due to the different electric distances. The center-of-inertia (COI) frequency is not suitable to represent frequency on buses in any places [4,5]. For example, the nodal frequency records show different trends in ESPOO and HERSLEV after a 580 MW disturbance in the Nordic power systems [6]. The influences of networks on frequency stability are considered, and the frequency indices are various in different areas [7]. Research discovers the frequency dynamics in large-scale power systems and reveals their spatial–temporal characteristics [8]. Federico Milano has made theoretical and practical studies on the frequency-difference phenomena in power systems' transient

processes. He provides solutions on how to estimate and calculate the nodal frequencies [9–11]. Researchers propose or use the method *frequency divider* to estimate the frequency on buses of a transmission system [9,12–14]. The authors have verified the formula in practical grids. The frequency divider is integrated into transient stability models considering spatial frequency variations on buses [15]. Researchers also study inter-area frequency oscillations, and distinct regional frequency phenomena [16]. The above research analyzes the phenomenon of nodal frequency difference in the transient processes but does not put forward solutions to solve frequency problems.

Energy storage is one of the best solutions for the frequency problems [17,18]. Primary regulation is one of basic functions for variable energy storage systems. The traditional energy storage system includes electro-chemical energy storage, flywheels, super capacitors [19, 20]. Also, virtual power plant (VPP) are popular to provide multiple auxiliary services. For example, virtual energy storage systems provide frequency regulations by coordinating demand responses and flywheels [21]. Distributed energy resources are aggregated to provide contingency frequency support via the virtual power plant technology [18,22,23]. Some researchers estimate the equivalent inertia and fast frequency responses of VPPs [24]. Furthermore, VPP provides
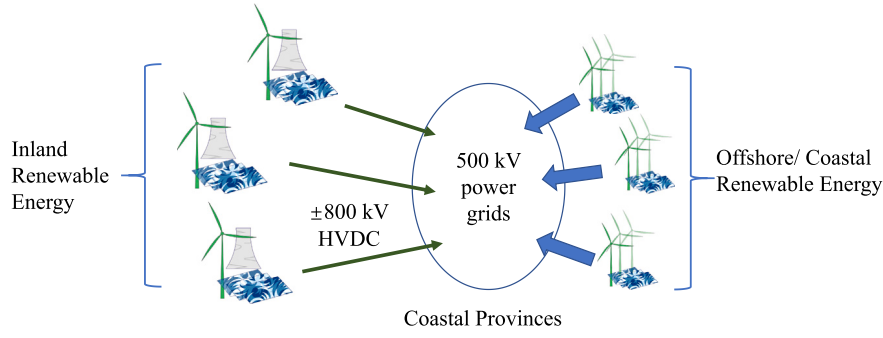

Fig. 1. The structure of coastal provinces' power systems in China.

frequency regulations by coordinating distributed battery storage and heat pumps [25]. The concept of energy storage in this paper contains both traditional energy storage and VPPs which provides primary regulation services.

Energy storage systems, including VPPs, provide primary regulations according to their local frequency deviations. The droop coefficients K_{sto} decide the magnitudes of energy storage's power responses against frequency deviations. Thus, it is significant to set proper energy storage droop coefficients considering various operating modes. For example, heuristic methods are used to design the coefficients. A genetic algorithm is proposed to determine the optimal frequency controller parameters to obtain a good frequency response [26]. An adjustment algorithm is proposed to solve the parameter design problem to improve the damping ratio [27]. A reinforcement learning-based controller with stability guarantees is designed to provide optimal primary frequency response [28]. A distributed averaging-based integral control method is proposed to achieve a better frequency response [29]. A paper discusses how to place hierarchical under-frequency load shedding for interconnected grids with communications [30]. However, the methods mentioned above cannot consider the influence of the operating modes. Also, practical energy storage and VPPs may be unable to support the complicated parameter design.

The center-of-inertia frequency response models are common in the following research. First, some research focuses on energy storage's contribution to frequency stability. Second, frequency-constrained co-planning of units and energy storage are discussed [31]. Third, a paper makes sizing for energy storage participating inertial response and primary frequency regulation [32]. Fourth, a study investigates the storage's contribution to wind-integrated systems under frequency constraints [33]. Finally, researchers figure out the frequency-constrained unit commitment problems considering energy storage [34]. Those papers merely use the COI frequency response models. We will show they are only suitable for small-scale power systems.

Many researchers consider the power grids for frequency response models instead of using COI ones. Some researchers discover the optimal virtual inertia placements using frequencies on rotational generators [5]. The research provides the DC swing equations considering power grids. The researcher studies the problem of virtual inertia placements and fast frequency responses and verified in Australian power systems [35]. The $\mathcal{H}_2$ norm is the optimization objective in Refs. [5] and [35]. Also, a group investigates the MPC-Based inverter power control to provide frequency support and studies the generators' frequency differences [36]. It minimizes all machine frequency deviations and rate of change of frequency (RoCoFs) but does not consider the nadir constraints. The research on energy storage placements considering nodal frequency responses is at the beginning, and there are only a few pieces of literature on this topic.

The frequency response models are too complicated for analytical methods when considering the grid, nodal frequency, and practical turbine models. Therefore, we seek machine learning algorithms to solve droop coefficient placement problems. A paper uses deep neural networks to predict the frequency response and embed the model into unit commitments [37]. Researchers propose an optimal classification tree for frequency-constrained unit commitments [38]. Several studies use deep learning, and sparse oblique decision trees for building security rules in power system operations [39–41]. Energy storage can be placed on any bus. Thus, the combinations of droop coefficients are continuous and high-dimensional, which makes previous algorithms difficult. This paper uses the alternative support vector machine trees (ASVMTREE) [42], developed by the same authors, to make accurate rule extractions for frequency dynamics.

The low nodal frequency nadirs significantly influence power supply quality for common electricity consumers. The current paper aims to solve the grid-side *frequency nadir problems* with suitable placements of storage droop coefficients. The operators should keep the *frequency nadirs* at each node within a set restriction, such as 0.5 Hz.

The paper's major contribution includes:

- Build and make simulations on a frequency response model considering units' and nodal frequencies.
- Make samplings and extract accurate rules for nodal frequency *nadir* constraints considering energy storage's primary regulations.
- Provide reliable droop coefficient placement solutions through rule embedding and optimizations.

The remainder of the paper is organized as follows. Section 2 is the motivations and framework. Section 3 introduces the frequency response model. Section 4 discusses sampling and rule extraction methods. Section 5 shows the optimization for droop coefficient placements. Section 6 verifies the proposed methods on modified IEEE 39- and 118-bus test cases. Finally, Section 7 concludes the paper.

2. Motivations and framework

2.1. Motivations: Nodal vs. COI frequency

The equivalent disturbances on generators at different locations vary when considering the power grid characteristics. In short, the units with shorter electric distances to the failure points get more significant impacts. Also, units require diverse time to recover revs (frequency) with the difference in inertia and primary regulation performances. The concept of *Frequency Divider* informs that the nodal frequencies are the superposition of rotation units' rotational speeds (frequency) related to electric distances [4,9]. As a result, the local frequency nadirs near the units with heavy disturbances and weak recovery ability will be much lower than that of the COI frequency.

Figs. 2 and 3 show the nodal frequency responses in IEEE 39- and 118-bus cases, respectively. The red dashes are the COI frequency curves. The local nadirs are lower than COI ones. Therefore, the COI frequencies are not suitable for large power grids against large disturbances.
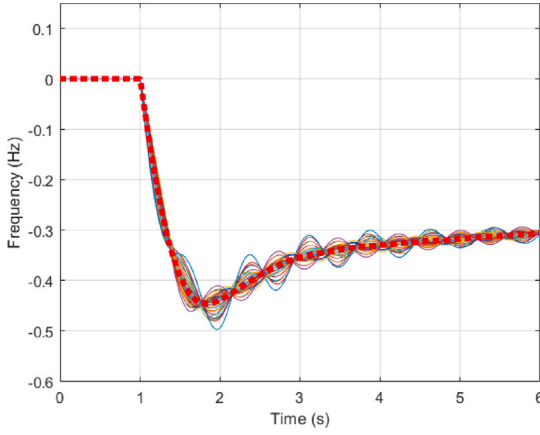
Fig. 2. 800 MW disturbances in modified IEEE 39-bus systems.
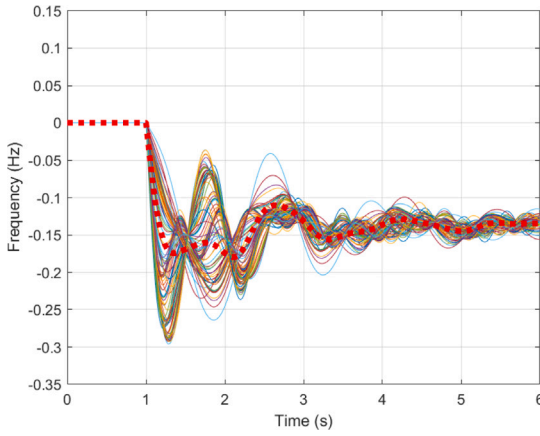

Fig. 3. 1500 MW disturbances in modified IEEE 118-bus systems.

In the meantime, the grid-side energy storage responds to the local frequency deviations and provides primary regulation services. The droop coefficient K_{sto} decides the energy storage's power responses to the frequency deviations, as shown in Eqs. (1) and (2). Note that we define the droop coefficient as the reciprocal of the classical form, as shown in Eq. (2). K_{sto} directly impacts the power system's frequency response characteristics. It also instructs energy storage planning and installations.

$$\Delta P_{sto} = -K_{sto}\Delta\omega \tag{1}$$

$$K_{sto} := -\frac{\Delta P}{S_0}\bigg/\frac{\Delta f}{f_0} = \frac{1}{R} \tag{2}$$

The difference in nodal frequency influences the storage reactions and contribution to nodal frequency nadirs. Therefore, the traditional COI frequency constraints are unsuitable for droop coefficient placement problems.

2.2. Framework

Fig. 4 depicts the framework of the proposed method. First, we calculate the typical operating modes through unit commitments for different load, wind, and solar power combinations (Section 4.1). Then, we make samplings on primary regulation parameters using the complete frequency response model (Section 4.2). The model considers both grid and generator characteristics. The energy storage responds to nodal frequency deviations. After that, we extract decision-tree-like rules with ASVMTREE and embed them into droop coefficient

placement models (Section 4.3/4). Finally, we get the optimization results and verify them by simulations (Section 5).

3. Frequency response models

3.1. Control models overview

A complete electro-mechanical transient simulation system may include comprehensive generator/ power electronic models and AC power flow. However, The simulation speed of the complete model is slow, and it faces reactive power configuration problems. In power system dynamics, the balance and control of active power are closely related to frequency response, while the influence of reactive power changes on power system frequency is limited. As a result, by ignoring some reactive power-related models and formulas, we can get a concise and fast simulation model.

Specifically, we simplify the generator models to second-order ones, neglect the voltage control (Automatic Voltage Regulation, AVR and Power System Stabilizer, PSS systems), and replace the AC power flow with DC ones compared with complete AC models. In the test case section (Section 6.5.1), we will show that the proposed frequency response model is accurate compared with the complete AC model.

Fig. 5 shows the frequency response models of conventional units and energy storage after step disturbances. We consider the characters of the power grid in the swing equations. The conventional units, including coal-fired (both primary and secondary reheat units), hydro- and gas-fired ones, provide primary regulations according to their rotating speeds. We take the governor dead bands and saturations into consideration. Also, the energy storage provides primary regulation services responding to the frequency deviations at its access point. The current research neglects the grid-forming (GFM) power electronic devices. We assume all renewable energy resources have zero inertia. The nodal frequencies are calculated through frequency divider methods, indicating they are a superposition of rotating generators. We regard all energy storage as ideal grid-following devices and ignore their direct contribution to nodal frequencies. The energy storage usually has less impact on nodal frequencies than conventional units in HVDC receiver-side power grids.

Our current method supports considering both droop and inertia in the energy storage model. However, the auxiliary services markets for energy storage's primary regulation are more mature than virtual inertia services. Distributed energy resources, electric vehicles, data centers, and virtual power plants can provide primary frequency regulations. Besides, it is challenging to set a proper virtual inertia for energy storage, since the nodal RoCoF would be much greater than the COI ones. In industry, the synchronous condensers (SynCon) are more popular for rotational inertia in High Voltage Direct Current (HVDC) projects. As a result, we only consider the droop controls in the current paper.

Furthermore, we do not consider grid-forming devices. There are only a few grid-side GFM energy storage operations in real-world power systems. Yet, the majority of power electronics run in grid-following modes and have the potential to provide primary regulations. Besides, GFM energy storage systems are more suitable for deployment in weak grids, such as centralized renewable power plants and weak transmission/distribution networks. The power capacity, maximum over-current capacity, and virtual inertia of operating GFM energy storage are significantly smaller than conventional units in primary transmission networks. After large disturbances, they easily lose synchronizations during violent power angle and frequency oscillations [43].
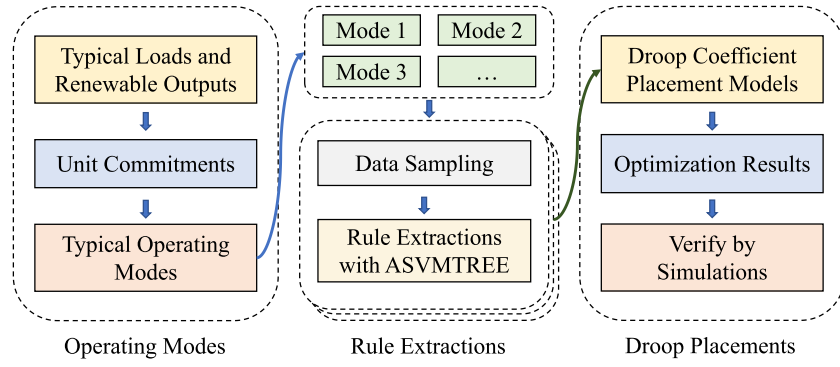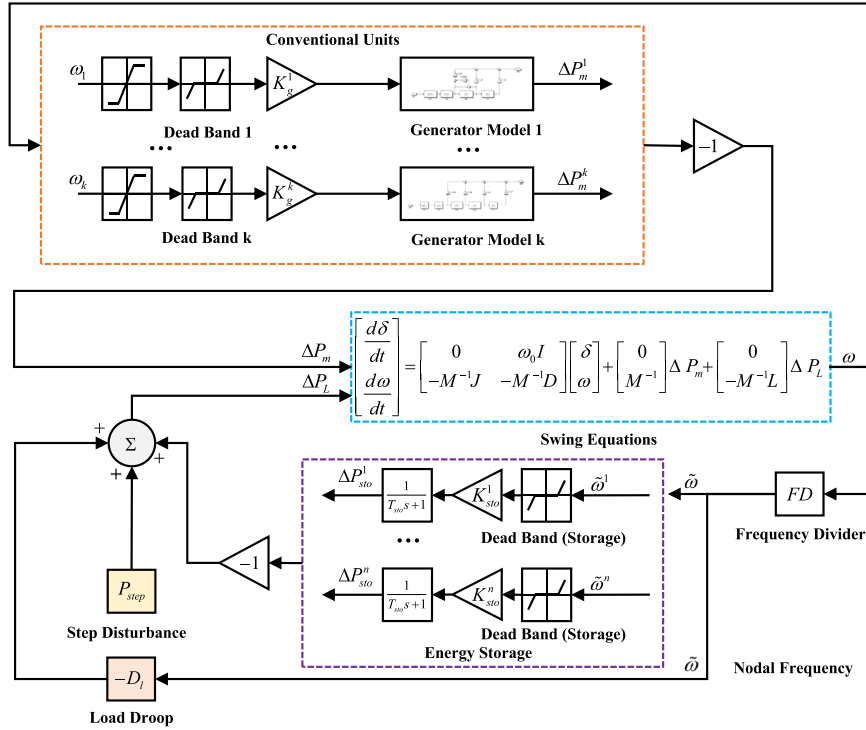
Fig. 4. The framework of the proposed method.

Fig. 5. Frequency response models.

3.2. Swing equations

The swing equations describe the generators' rotor angles and rotating speeds after disturbances based on DC power flow assumptions [5, 36]. Eqs. (3) and (4) are the transient state DC power flow formula, and Eqs. (5) and (6) are units' swing equations. Eq. (7) is the swing equation considering grid characteristics. g, L represent generator and load buses, respectively.

$$\begin{bmatrix} \Delta P_g \\ \Delta P_L \end{bmatrix} = \begin{bmatrix} B_{gg} & B_{gL} \\ B_{Lg} & B_{LL} \end{bmatrix} \begin{bmatrix} \Delta \delta \\ \Delta \theta \end{bmatrix} \tag{3}$$

$$\Delta P_g = \left(B_{gg} - B_{gL} B_{LL}^{-1} B_{Lg} \right) \Delta \delta + B_{gL} B_{LL}^{-1} \Delta P_L \tag{4}$$

δ and θ are unit rotor angles and nodal phase angles. The matrix $\begin{bmatrix} B_{gg} & B_{gL} \\ B_{Lg} & B_{LL} \end{bmatrix}$ is the augmentation of the DC nodal admittance matrix with generators' transient impedance branches. B_{gg} is a diagonal matrix with elements equal to the reciprocal of units' transient impedance $1/x_d'$. $1/x_d'$ are different for generators in various turbines and capacities. B_{LL} is a sum of B_{gg} and original DC nodal admittance matrix. B_{gL} and B_{Lg} are admittance between generators and the grid. We define

$J = B_{gg} - B_{gL} B_{LL}^{-1} B_{Lg}$ and $L = B_{gL} B_{LL}^{-1}$ for short. In calculating the transient state, the complete DC power flow formula includes both the steady and transient parts. However, the power and angles in the steady states are considered constant values determined by the systems' unit commitment results. As a result, they do not influence the frequency response characteristics in transient states (under DC power flow assumptions). Therefore, we only use the transient part, i.e., Eq. (4), to derive swing equations.

Eqs. (5) and (6) are each unit's swing equations without power grids. ω are the normalized deviations of units' rotation speeds. ω_0 is the standard speed (frequency), equivalent to 50 Hz. M are the units' inertia. ΔP_m and ΔP_g are deviations of units' mechanical and electromagnetic power. D is the damping parameter set as 2% for conventional units. In this paper, the power-related values are normalized by 100 MVA.

$$M \left[\frac{d\omega}{dt} \right] = \Delta P_m - \Delta P_g - D\omega \tag{5}$$

$$\left[\frac{d\delta}{dt} \right] = \omega_0 \omega \tag{6}$$

Substitute Eqs. (5) and (6) into (4), then we finally have the swing equations considering power grids, as shown in Eq. (7).

$$
\begin{bmatrix} \frac{d\delta}{dt} \\ \frac{d\omega}{dt} \end{bmatrix} = \begin{bmatrix} 0 & \omega_0 I \\ -M^{-1}J & -M^{-1}D \end{bmatrix} \begin{bmatrix} \delta \\ \omega \end{bmatrix} \\ + \begin{bmatrix} 0 \\ M^{-1} \end{bmatrix} \Delta P_m + \begin{bmatrix} 0 \\ -M^{-1}L \end{bmatrix} \Delta P_L
$$
(7)

3.3. Frequency divider and energy storage regulations

Eq. (8) is the nodal frequency divider formula, which calculates the nodal frequencies with generators' frequencies [4,9,14]. The matrix $-B_{LL}^{-1}B_{Lg}$ is short as $[FD]$.

$$
\tilde{\omega} = -B_{LL}^{-1}B_{Lg}\omega = [FD]\omega
$$
(8)

The energy storage provides primary regulations according to their local frequencies. K_{sto} is the droop coefficient to be determined when placing energy storage. The storage's power adjustments are Eq. (9). The energy storage's dead bands are ± 0.02 Hz. T_{sto} is 0.2 s.

$$
\Delta P_{sto} = \frac{K_{sto}}{T_{sto}s + 1}\tilde{\omega}
$$
(9)

The T_{sto} is set as 0.2 s for three purposes. (1) Consider the control delay set by centralized control stations. (2) Improve the stability of energy storage power outputs. (3) Avoid unreliable PLL measurements 0–100 ms after the disturbances. Many devices can reach the 0.2-second control delay, e.g., centralized and distributed energy storage stations, electric vehicles, the backup battery in base stations, and computing clusters. Furthermore, the virtual power plant technology can coordinate various distributed energy resources to provide primary regulations.

Also, the droop character of nodal power loads $-D_l$ are set as 1% of their minimum values. Energy storage, load, and step disturbances P_{step} consist ΔP_L in the swing equations.

3.4. Conventional units primary regulations

The conventional units include thermal and hydro turbines (GH). In addition, primary reheat (TB), secondary reheat (TC), and gas-fired (TG) generators are three kinds of typical thermal units. The industry-level generator models $G(s)$ are from a professional software PSD-ST as shown in Appendix [44]. The data-driven methods make it possible to use more complicated and industrial models instead of simplified ones in previous research [45].

We set a 0.5-second delay for primary reheat (TB) and secondary reheat (TC) units. The conventional units' regulations are Eq. (10) when neglecting the dead bands and delay components. K_g is the droop coefficient of the conventional unit. ΔP_m is the mechanical power of primary regulation responses from a conventional unit. ω is the frequency deviation.

$$
\Delta P_m = G(s)K_g\omega
$$
(10)

In the current research, we do not consider the detail models of PSS and AVR. However, we retain the interface of the PSS systems in simulation models for industry-orientated studies, and our methods are still suitable.

3.5. Disturbance

We assume the largest disturbances are from the failure of high-voltage cross-regional transmission injections. The disturbances are 800 MW and 1500 MW for modified IEEE 39- and 118-bus test cases. There are two individual injections in IEEE 39- and 118-bus systems at different access points. When injections fail, the *frequency nadirs* should not exceed **0.5 Hz and 0.3 Hz**, respectively.

3.6. Discussions

The reasons we do not use higher-order AC models directly are threefold: (1) The speed of AC model simulations visibly slows down, as the network scales and the number of units increases. (2) The numerical stability of the AC model is poorer than the proposed model. The AC models get accurate simulation results by solving differential–algebraic equations (DAE). Otherwise, the proposed method only relies on ordinary differential equation (ODE) solvers. ODE's computing speed and stability are significantly better than DAE's. (3) We should set proper voltage/reactive power values to initialize the simulations for AC models. It relies on a complex non-linear optimization.

The current paper combines the Frequency Divider theories to estimate the nodal frequency from the rotational speeds of conventional units. The Frequency Divider theories have been verified in AC simulations and hardware models. It also performs well with the simplified swing model, i.e., Eq. (7). Also, we do not need to neglect any non-linear blocks in simulation models. Our method reduces the difficulties of simulations while increasing the simulation results' robustness.

The model works well to simulate the systems' responses after active-power-dominated disturbances. For example, the model can describe HVDC/ generator failures, line trips, and active power responses from distributed energy resources. Also, the model is able to simulate the unit/devices' recovery behaviors, such as primary/secondary regulations and damping characteristics. Since the model assumes the voltage magnitudes of power systems are around 1.0 p.u., the model is unsuitable for reactive power disturbances and short circuits. The voltage changes rapidly in those situations, and we cannot regard them as static values.

The frequency response model's complexity makes traditional analytical methods challenging to be embedded into optimization models. Therefore, we use data-driven algorithms to extract rules from simulations of massive coefficient placement plans, as introduced in the following section.

4. Data sampling and rule extractions

The sampling and learning procedure structure is shown in Fig. 6. There are four steps in this section, i.e., typical operating modes generations, data sampling, rule extractions, and embedding.

For example, there are 16 operating modes generated by unit commitments. Also, there are two possible locations for large disturbances. Then, we make droop coefficient samplings on the $16 \times 2 = 32$ operating and disturbance modes. Then, ASVMTREE extracts 32 rules in total for energy storage placements. Finally, we embed the rules into optimization problems.

4.1. Typical operating (online) modes

The conventional units' online conditions critically influence the power systems' frequency response performances. We study power systems with high renewable and cross-regional power injections. We build typical operating modes using daily unit commitments under different power loads, and wind and solar power outputs.

The unit commitments minimize the economic cost considering the following constraints:

- power balances and online backups
- start-up and shut-down constraints
- minimum and maximum power outputs
- branch power flow limits
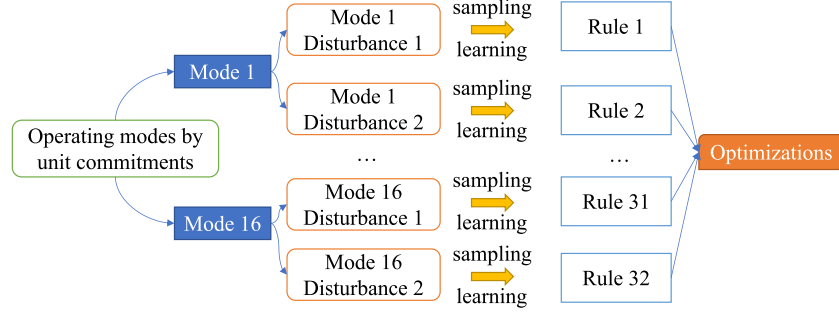- center-of-inertia RoCoF constraints, set as 1 Hz/s.

Fig. 6. The workflow of data sampling and rule extractions.

The thermal generators in China can climb 2–2.5% per minute, so the ramp limits for hours are neglected.

In test case, we have total typical power loads $load = [l_1, \ldots, l_l]$, solar power outputs $solar = [s_1, \ldots, s_s]$ and wind power outputs $wind = [w_1, \ldots, w_w]$. We traverse the typical values of the load, solar, and wind and make $l \cdot s \cdot w$ different unit commitments. Then, we sort the unique unit online conditions (labeled as P_x^k for kth condition) according to their occurrence rates (labeled as p_{uc}^k). After that, we select several highest occurrence-rate online conditions and build simulation samples for rule extractions. We should make simulations on each cross-regional injection in every unit online condition.

4.2. Data sampling

In our model, all load buses can place primary regulation energy storage devices. Therefore, it is impossible to traverse all possible K_{sto} plans and make simulations due to a large number of buses.

In this paper, we require the thresholds of nodal frequency nadirs to be *0.5 Hz, IEEE 39* or *0.3 Hz, IEEE 118* on all buses. Thus the minimum nodal nadirs in the simulation datasets should be close to 0.5 Hz (0.3 Hz), the frequency restriction. Because the massive simulations are time-consuming, it is necessary to design a strategy so that every sample contributes to rule extractions as far as possible. We build suitable simulation datasets with the two steps below.

4.2.1. Initial distribution and line search

The simulation's n-dimension input vector consists of the primary regulation parameter K_{sto}^n, $n = 1, \ldots, N$ on each bus. n is the number of buses. The contribution of energy storage is generally complementary in different locations, especially in small grids. For example, the nodal frequencies are close to COI ones in the IEEE 39-bus test case, as shown in Fig. 2. As a result, we expect the distribution of the sum of $K_{sto} = [K_{sto}^1, \ldots, K_{sto}^N]^T$, i.e., $\sum_{n=1}^N K_{sto}^n$, should not be too large. The distributions of K_{sto}^n are supposed to have a feature of long tails. The mean values of distribution will not be too large, while the span range of samples is sufficient.

We select the folded normal distribution $K_{sto}^n \sim N_f(\sigma)$, the absolute values of the normal distribution $N(0, \sigma)$ as the initial one. σ is the standard deviation. Eq. (11) is the probability density function.

$$f(x, \sigma) = \frac{1}{\sigma\sqrt{\pi/2}} \exp\left[-\frac{1}{2}(x/\sigma)^2\right], \quad x \geq 0 \tag{11}$$

Then, we use a variable step line search to find suitable σ for initial datasets. We assume the datasets are acceptable when the value of the empirical cumulative distribution function at 0.5 Hz (i.e., $\Phi(0.5)$, IEEE 39) or 0.3 Hz (i.e., $\Phi(0.3)$, IEEE 118) is within $0.3 \sim 0.7$. The algorithm is shown in Alg. 1. One hundred samples are simulated in each step through the Latin hypercube sampling.

We start simulating and building datasets for rule extractions using the σ from line search. In this problem, 2000 samples adequately describe the preliminary frequency response characteristics.

Algorithm 1 Variable step line search

Input: Initial sigma σ_0, initial step s_0
  Initial values: $\sigma = \sigma_0$, $s = s_0$, last = -1
  while flag == 0 **do**
    datasets = simulate(σ); cdf = $\Phi_{datasets}(0.5)$;
    if 0.3<cdf<0.7 **then** flag =1; **return** σ
    else if cdf≤0.3 **then**
      if last == 0 **then** $s = s >> 1$
      end if
      $\sigma = \sigma + s$; last = 1;
    else
      if last == 1 **then** $s = s << 1$
      end if
      $\sigma = \sigma - s$; last = 0;
    end if
  end while

4.2.2. Salt projections with SVM

To enhance the reliability of simulation results, we hope the samples are close to the boundaries of frequency restrictions, 0.5 Hz (0.3 Hz). As a result, we utilize linear support vector machines (SVM) to learn the 0.5 Hz (0.3 Hz) cut planes from the datasets in Section 4.2.1. The cut plane has a form of Eq. (12). a and b describe a linear cut plane. $K_{sto}^i, i = 1, \ldots, n$ are droop coefficients on bus i.

$$a^T x + b = 0, \quad x = [K_{sto}^1, \ldots, K_{sto}^n]^T \tag{12}$$

In frequency response problems, the accuracy of linear SVM is usually greater than 85%. The nadirs of samples on or nearby the cut planes are much closer to 0.5 Hz (0.3 Hz) than in Section 4.2.1. Therefore, we can project the vectors in datasets to the cut plane using projection transform in Eq. (13). x' and x are samples after and before the transformation.

$$x' = x - \frac{(a^T x + b)a}{a^T a} \tag{13}$$

After that, we add salts, i.e., some disturbances to the x's, to make them fill the space near the boundary. Uniform distribution salts in the range of $[-25\%, 25\%]$ are added to each dimension in x'. Then, we simulate the x' to enrich the datasets. If the probability of the nadirs of x' within 0.5 ± 0.1 Hz (0.3 ± 0.1 Hz) is larger than 90% ($gaprate$), x' and x consist of the final datasets for extractions. Otherwise, we will repeat the step in this section and build another 2000 samples to increase the sampling density nearby the boundaries. Fig. 7 shows an example of samples in modified IEEE 118-bus test cases. The first 2000 samples are built with the method in Section 4.2.1, and the last 2000 ones use salt projections. The distribution of frequency nadirs in the last 2000 samples is much narrower than the first ones. The algorithm is shown in Alg. 2.

4.2.3. Discussions

The sampling strategy is critical for the effectiveness of extracted rules. The strategy design should be based on the characteristics of
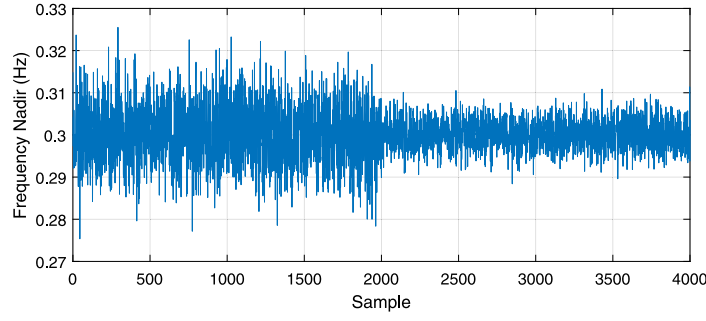
Fig. 7. Frequency nadirs of samples in modified IEEE 118-bus test cases.

Algorithm 2 Sampling with salt projections

Input: Initial 2000 samples, set_0

$gaprate = 0$, $k = 0$

while ($gaprate \leq 0.9$ and $k < 3$) or $k < 2$ **do**

    $cpf = svm(\cup_{i=0}^{k} set_i)$;   # SVM classification

    $x' = \text{salt\_project}(cpf, set_k)$;   # Salt projection

    $set_{k+1} = \text{simulation}(x')$;   # New simulations

    $gaprate = gaprate(set_{k+1})$; k++; # Renew $gaprate$

end while
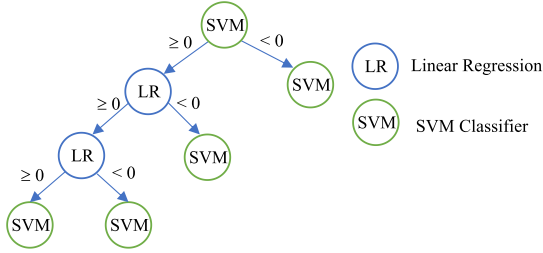
Fig. 8. Structure of alternate support vector machine decision trees.

the target problem. The current sampling method is applicable to the test cases in this paper. We further discuss the improvements in the sampling strategy to cope with general problems in Section 6.5.2. We introduce the sampling solutions for various power system models, initial states, and potential results.

4.3. Rule extractions

We make rule extractions with alternate support vector machine decision trees (ASVMTREE), a classification model. The algorithm is suitable for power systems rule extractions in many disciplines, such as frequency, voltage, N-1, transient stability problems, and multi-energy systems [42].

We assume the classification label is 1 when the minimum frequency nadir is equal to or smaller than 0.5 Hz (0.3 Hz) and 0 otherwise. In practice, we remove the datasets whose minimum nadirs are within 0.5 ± 0.002 Hz (0.3 ± 0.002 Hz) to avoid over-fits.

4.3.1. Alternate support vector machine decision trees

The alternate support vector machine decision trees combine machine learning algorithms, support vector machine (SVM), and linear regression (LR) into decision tree structures. The SVM classifier consists of the leaf nodes, while non-leaf nodes can be linear regression (major) and SVM classifier, as shown in Fig. 8.

The traditional decision tree classifiers build models by heuristically splitting nodes at the variable's best dimension evaluated by the Gini index. The binary trees can be easily converted into MILP ones for optimization problems. Many researchers improve the decision trees
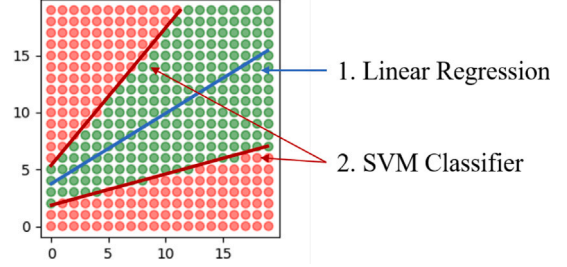

Fig. 9. Example of linear inseparable problem and solutions.

by changing the splitting rules to a cut plane instead of the best dimension [39,46]. A common way to find cut planes is through support vector machine classifiers. It provides the best optimal separating hyperplane like $a^T x + b = 0$. The linear forms can be embedded in optimization models using big M methods [39].

However, support vector machines might face linear inseparable problems and fail to separate datasets. For example, there are many positive (green) samples between negative (red) ones, as shown in Fig. 9. It is difficult for linear SVM classifiers to make classifications. We cut the green region into two parts using linear regression. Then, linear SVM classifiers can separate positive and negative samples into two parts. As a result, a linear regression can easily solve the linear inseparable problems.

We call the method the alternate support vector machine decision trees (ASVMTREE). The node split strategy's kernel part is shown in Alg. 3. The $ACC(depth)$ determines whether linear regression or support vector machine is suitable to construct cut planes, as shown in Eq. (14). $ac(0)$ is the accuracy of the SVM classifier at depth 0. $ACC(0) = ac(0)$ makes the root node a SVM classifier. We will not use linear regression when SVM accuracy is greater than 0.96 to avoid possible over-fittings.

$$ACC(depth) = \min(ac(0) + 0.05 \cdot depth, 0.96) \tag{14}$$

The ASVMTREE's detailed information on the algorithm explanations and performances can be found in [42]. In our test, linear support vector machines' accuracy is above 90%. ASVMTREE inherits good performances from support vector machines and is thus a good choice for nodal frequency constraints. The ASVMTREE degenerates into the linear support vector machine in simple datasets. Meanwhile, it significantly improves the accuracy for datasets that linear support vector machines cannot make accurate classifications.

4.4. Rule embedding

Both linear support vector machine classifiers and linear regression results are in a linear form, i.e., $a^T x + b = 0$. $a^T x + b \geq 0$ represents the left branch or positive results, and vice versa. We can write the constraints of positive leaves (classified as 1) as combinations of linear constraints on their route to the root. The matrix A_i and B_i combines

Algorithm 3 Node Split Strategy in ASVMTREE

Input: label y, input variable X, depth $depth$
  function NODE_SPLIT(X, y, $depth$)
    clf, y_pred = **SVC**.fit_predict(X, y)
    # **SVC**: linear support vector machine classier
    cur_gini = gini(y_pred, y) # Gini index
    if accuracy_score(clf)<ACC($depth$) **then**
      k_select=random.choice(MK)
      # randomly select MK dimensions, 8 suggested
      delta_gini = Inf
      for k in k_select **do**
        clft, X_pos, X_neg = **LR**.fit_predict()
        # **LR**: linear regression
        clf1, y_pred1 = **SVC**.fit_predict(X_pos, y_pos)
        clf2, y_pred2 = **SVC**.fit_predict(X_neg, y_neg)
        delta_gini_cur = delta_gini(clft, clf1, clf2)
        if delta_gini_cur < delta_gini **then**
          k_select = k, clf = clft
        end if
      end for
    end if
    return clf   # **LR** or **SVC** results, cut planes
  end function

nodes' a and b on the route of positive leaf i, as shown in Eq. (15). We should take the opposite number of a and b when the nodes' labels are less-than (<). The method is similar in Ref. [39].

$$A_i^T x + B_i \geq -M \cdot (1 - m_i), \quad i = 1, \ldots, l \tag{15}$$

$$\sum_{i=1}^{l} m_i \geq 1 \tag{16}$$

Assuming there are l positive leaves, we can combine them using big M methods, as shown in Eqs. (15) and (16). M is a large positive number, and m_i are integers. $m_i = 1$ means the input x obey the rules of leaf i.

4.4.1. Improvements compared with the previous research

First, we develop a useful data sampling method to assist ASVMTREE in rule extractions. There are two major steps, i.e., Initial Distribution and Line Search (Section 4.2.1) and Salt Projections with SVM (Section 4.2.2). The data samples are closer to the 0–1 boundaries. The data efficiency is significantly higher than that of traditional uniform sampling. Ref. [42] merely introduces the machine learning algorithm, not the sampling methods.

Second, we embed the extracted rules into the optimization model and verified that the ASVMTREE is suitable for practical problems in power systems. Ref. [42] points out that the extracted rules can be converted to MILP constraints, while the current paper achieves the proposal.

5. Droop coefficient placements

5.1. Optimization objectives

As time goes, the nodal frequencies will be close and equal to the COI one. The final system frequency ($\Delta f|_{t \to \infty}$) would be Eq. (17). K_{unit} and K_{sto} are the primary regulation parameters of conventional units and energy storage. ΔP is the magnitude of disturbance. As a result, too much K_{sto} may waste the fast regulation resources.

$$\Delta f|_{t \to \infty} = \frac{\Delta P}{\sum K_{sto} + \sum K_{unit}} \tag{17}$$

The optimization objective of droop coefficient placements is to minimize the droop coefficients of energy storage $\sum K_{sto}$. We assume the energy storage resources derive from the following three types: (1)

The primary regulation from existing energy storage or other power electronic facilities; (2) Fixed assets (usually by investments), the energy storage that is long-term deployed in the power systems; (3) Movable assets (usually market-oriented), the energy storage operates in several of operation modes. The energy storage could be in form of both centralized/distributed energy systems and various virtual power plants. Especially, the deployments of type 3 energy storage are related to the power system modes. The virtual power plant companies control and aggregate massive distributed energy resources spreading the grids. The power system operator may sign day-head contracts for primary regulations with VPP owners.

The droop coefficients are labeled as $K_{sto,e}$, $K_{sto,c}$, and $K_{sto,m}$ for the above three types. $K_{sto,c}^{max}$ is the maximum $K_{sto,c}$ at each bus. We encourage more fixed energy storage in the power systems instead of movable ones. We assume the costs of type 3 are **three times** of type 2's.

The problem's optimization objective includes the costs of type 2 and 3 energy storage and penalties on operation modes, as shown in Eq. (18). $pindex = [pindex^1, \ldots, pindex^K]$ are binary penalty variables for K operating modes. $pindex^k = 1$ means we cannot satisfy the constraints in the mode k. M is the large value in the big M method.

$$\min \sum_{k=1}^{K} K_{sto,c}^{max} + 3 \cdot \sum_{k=1}^{K} \sum_{n=1}^{N} K_{sto,m}^n \cdot p_{uc}^k + M \sum_{k=1}^{K} pindex^k \tag{18}$$

5.2. Constraints

Eqs. (19), (20) and (21) are the lower and upper constraints of K_{sto}. The total regulation parameter on buses $K_{sto,all}^k$ should obey the power systems' energy storage access requirements, i.e., below a maximum value K_{max}.

$$K_{sto,all}^k = K_{sto,e} + K_{sto,c} + K_{sto,m}^k \tag{19}$$

$$K_{sto,all}^k, K_{sto,c}, K_{sto,m}^k \geq 0, \quad K_{sto,c} \leq K_{sto,c}^{max} \tag{20}$$

$$K_{sto,all}^k \leq K_{max} \tag{21}$$

Also, Eqs. (22) and (23) are the nodal frequency nadir constraints as an extension of Eqs. (15) and (16). i, h, k represent different leaves, power injections, and online modes. $l^{h,k}$ is the number of leaves ASVMTREE for hth injections and mode k. The definitions of A, B, M, m are the same as Eq. (15).

$$A_{i,h,k}^T K_{sto,all}^k + B_{i,h,k} \geq -M \cdot (1 - m_{i,h,k}), \quad \forall i, \forall h, \forall k \tag{22}$$

$$\sum_{i=1}^{l^{h,k}} m_{i,h,k} \geq 1 - pindex^k, \quad \forall h, \forall k \tag{23}$$

In summary, the optimization objective Eqs. (18) and constraints Eqs. (19) to (23) are the mathematical form for the droop coefficient placements.

5.3. Verification by simulations

We bring the droop placement solutions back into simulation models and make verification on nodal frequency nadirs and RoCoFs. In some operating models and operating models, the nadirs may slightly exceed 0.5 Hz (0.3 Hz) limits. However, the maximum errors are usually around 0.01 Hz in test cases. Therefore, in practical uses, we can change rule extractions' 0.5 Hz (0.3 Hz) restrictions to a smaller value, e.g., 0.49 Hz (0.29 Hz). It can lead to more conservative results, guaranteeing all the nodal frequency nadirs within 0.5 Hz (0.3 Hz) restrictions. Also, we can mildly adjust the magnitudes of $B_{i,h,k}$ in Eq. (22) to reduce the small errors.
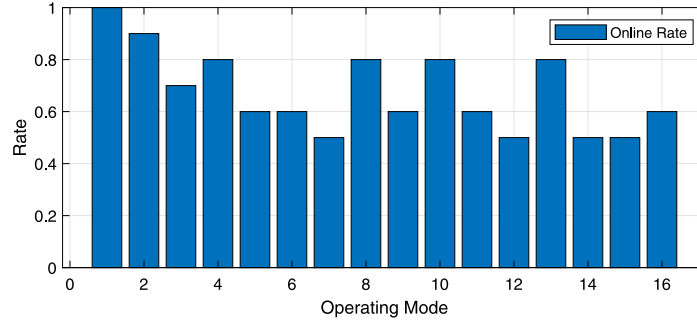
Fig. 10. Online rate of operating modes in IEEE 39-bus test case.

Table 1
Conventional unit parameters.

Index	1	2	3	4	5	6
Type	TB6	TC6	TB10	TC10	TG3	GH3
Frequency response						
Turbine	TB	TC	TB	TC	TG	GH
Capacity (MW)	667	667	1050	1050	300	300
Inertia constant (s)	6	8	10	10.6	9	10.5
x'_d	0.041	0.039	0.024	0.021	0.065	0.07
Dead band (Hz)	0.033	0.033	0.033	0.033	0.033	0.05
Time delay (s)	0.5	0.5	0.5	0.5	0	0
Unit commitment (costs in 10^4 RMB)						
Variable cost	0.021	0.02	0.019	0.017	0.025	0.001
Startup cost	30	30	100	100	0	0
Shutdown cost	30	30	100	100	0	0
Min on time	4	4	4	4	0	0
Min off time	8	8	8	8	0	0
Min power	0.25	0.4	0.4	0.4	0.2	0.01

Table 2
ASVMTREE's performances in each case.

Case	Time (s)	Accuracy	F1 score (positive)	F1 score (negative)
IEEE 39	0.06	99.67%	0.9965	0.9969
IEEE 118	0.67	99.85%	0.9985	0.9985

In the meantime, the grid-side RoCoF problems can be solved by adjusting the protection rules in engineering ways. E.g., the United Kingdom relaxes the average RoCoF limits to 1 Hz/s with 0.5 s time delay [48]. We will show the RoCoFs obey the regulations like the UK in most situations considering nadir limits only.

6.2. Performances of data sampling and rule extractions

6.2.1. Simulation time costs
The simulation costs are around 2 and 6 min for modified IEEE 39- and 118-bus test cases, 4000 samples per case. All buses are available to deploy energy storage. We make simulations on a workstation with Intel i9-10980XE CPU and 128 GB RAM, using Simulink and Parallel Computing Toolbox on MATLAB 2020b.

6.2.2. ASVMTREE performances
Table 2 shows the performances of ASVMTREE in each case, including the average time costs, accuracy, and F1 scores. The algorithm's high performances indicate that it is effective for energy storage droop coefficient placement problems.

6.3. IEEE 39-bus test case

There are five TB6, two TC6, two TG3, and one GH unit in the IEEE 39-bus systems. Two 800 MW cross-regional power injections are localized in buses 7 and 24. We scan power load (3.5 to 8 GW), solar (0.6 to 1.5 GW), and wind (0.6 to 1.5 GW) for unit commitments. We select the top 16 occurrence-rate operating modes to verify the proposed method. Fig. 10 shows the conventional unit's online rate in each operating mode. The grid topology and parameters are from MATPOWER. K_{max} is 100 in this case.

The parameters of type 1 are $K_{sto,e} = 5$ on each bus. Figs. 11 and 12 are the optimization results of type 2, 3's primary regulation parameters. The type 2 storage deploys near the power injection points (buses 31, 23, 36) and buses between the points (buses 28, 29, 38), as shown in Fig. 13. Type 3 storage is a supplement in different modes.

Besides, we make simulations on the 16 × 2 modes considering differed online modes and disturbance locations with the droop coefficients placement results. In Fig. 14, the minimum frequency nadirs are close to 0.5 Hz, the set value, and can be accepted considering possible
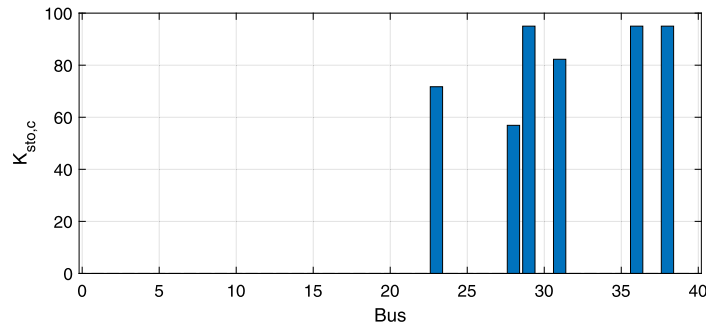
5.4. Capacity estimations

We may estimate the power capacity of energy storage after determining K_{sto} on buses. A possible method is to multiply the K_{sto}^i with nodal frequency nadir $f_{nadir}^{i,h}, \forall h$ on bus i, as shown in Eq. (24). P_{sto}^i is the estimated capacity of ith energy storage.

$$P_{sto}^i = -K_{sto}^i \cdot \max_h f_{nadir}^{i,h}, \quad \forall h, \forall i \tag{24}$$

The nodal frequency nadirs in some buses might be lower than cross-regional power injection failures, even though their absolute disturbance values are not as large. Therefore, we could do more simulations considering various possible disturbances—for example, N-1 failures and renewable blackouts.

6. Test cases

6.1. Unit parameters

We consider six typical conventional units; their parameters are shown in Table 1. The control models of the generators are shown in Appendix. We refer to the Power System Design Manual [47] for capacity parameters, inertia time constants, and transient reactance x'_d. We select *practical unit models* [44] instead of simplified ones in most research (such as [45]) to show the universality of the proposed methods. The method is suitable for models used in engineering rather than only acceptable for academic research. We verify the proposed method in modified IEEE 39- and 118-bus test cases.

It should be noticed that the method is still capable when each unit's parameters (including that in turbine models) are different. We choose the six typical models for the convenience of result presentations.

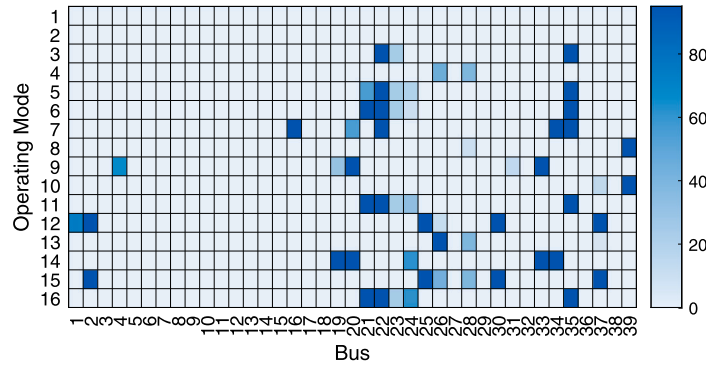**Fig. 11.** Droops of Type 2 energy storage in IEEE 39-bus test case.

Fig. 12. Droops of Type 3 energy storage in IEEE 39-bus test case.
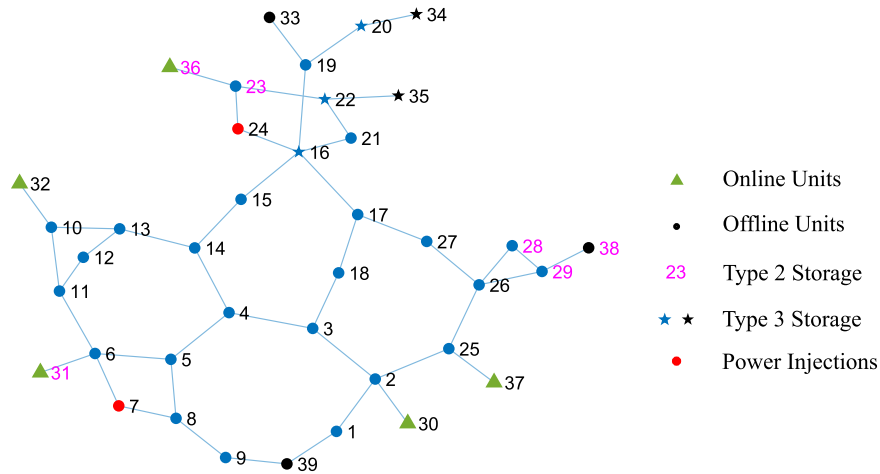

Fig. 13. Droop placements of IEEE 39-bus test case in operating mode 7 (the lowest online rate). Type 2 storage are on buses with magenta labels, while type 3 are on star-shaped buses. The red buses, 7 and 24 are cross-regional power injections. Units are online at green triangle-shaped buses.
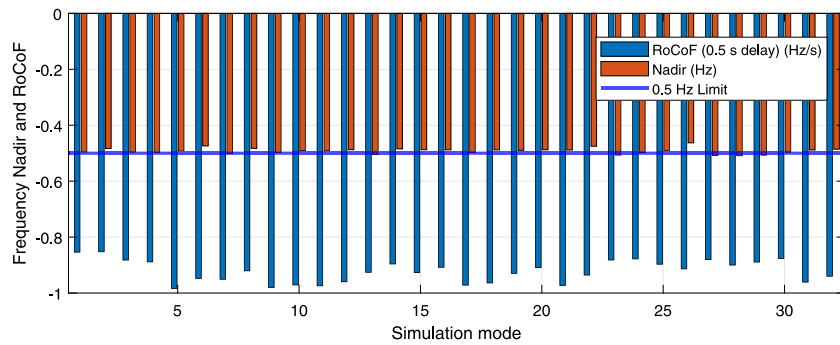

Fig. 14. Minimum frequency nadirs and RoCoF in IEEE 39-bus test case.
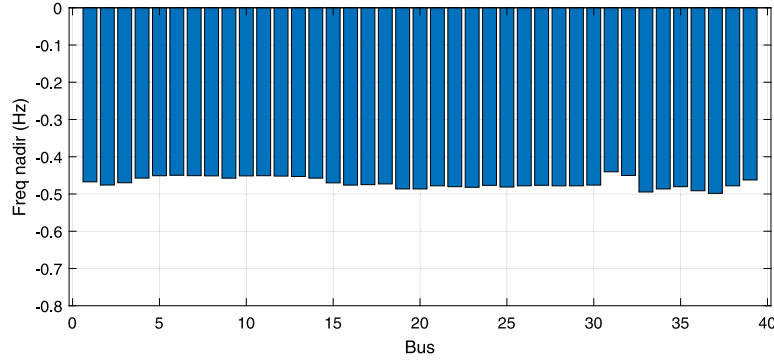
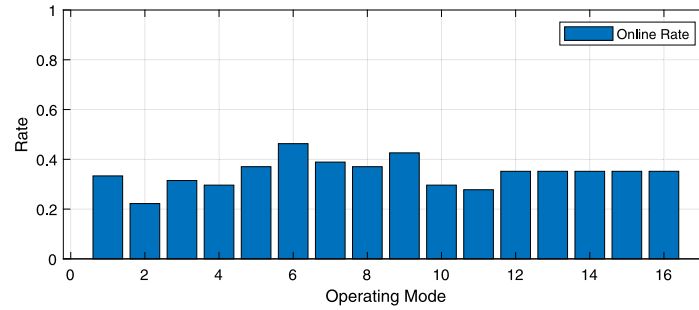**Fig. 15.** Example of nodal frequency nadirs in IEEE 39-bus test case.

Fig. 16. Online rate of operating modes in IEEE 118-bus test case.

measurement errors. The minimum RoCoF is less than 1 Hz/s with a 0.5-second delay in all situations, which obeys the UK's regulations.

As shown in Fig. 15, the nodal frequency nadirs are close among buses in a small system, the IEEE 39-bus test case. The maximum error is around 0.009 Hz (1.8%) at simulation mode 28. It is much better than the traditional analytic method (maximum error around 5%) that only considers COI frequency and simplified models [45]. The phenomena are similar in other small systems, such as the IEEE 89-bus test case (12 conventional units). It explains why COI frequencies are suitable in many pieces of research.

6.4. IEEE 118-bus test case

There are 54 conventional generators in the IEEE 118-bus test case, including 27×TB6, 9×TC6, 5×TB10, 2×TC10 and 11×TG3 in the system. Two 1.5 GW cross-regional injections are located in buses 49 and 37. We scan power load (8 to 12 GW), solar (1.5 to 2.5 GW), and wind (1.5 to 2.5 GW) for unit commitments. $K_{max} = 165$ in this case. We reduced the line impedance to 40% of that in the original IEEE 118-bus test case. It ensures that the grid has sufficient transmission capacity. The parameters of type 1 are $K_{sto,e} = 15$ on each bus to simulate the existing primary regulation resources, such as energy storage and power electronic converters on renewables. Type 1 energy storage systems are important components to support the frequency stability in low-inertia systems. The maximum droop for type 3 storage is set as 50, i.e., $K_{sto,c}^{max} = 50$, in this case. Fig. 16 shows the conventional unit's online rate in each operating mode. The typical modes consist of conventional units' higher and lower online rates.

Location of droop placements. Fig. 17 shows the droop placements of the IEEE 118-bus test case in operating mode 2, the lowest online rate. Droops of type 2 storage are placed near the power injection points, buses 37 and 49. The type 3 storage are located both near the disturbances and units as a supplementary.

Accuracy of the proposed method. The minimum frequency nadirs and RoCoF in IEEE 118-bus test case are shown in Fig. 18. The frequency nadirs are very close to and within the 0.3 Hz limits, and the RoCoF are within 1 Hz/s. The frequency nadir error is below 0.01 Hz, which is negligible in practical power systems.

Nodal frequency nadir differences. Fig. 19 shows an example of nodal frequency nadirs in the IEEE 118-bus test case with a 1500 MW disturbance at bus 37, operating mode 15. The frequency nadirs are different on each bus. The frequency nadirs are much lower on buses around the closest conventional units to the disturbances. The disturbance has fewer influences on buses far from the power injection points. As a result, it is crucial to consider nodal frequency instead of merely using COI frequencies. The COI frequency cannot guarantee each bus's frequency security.

Economic costs. Fig. 20 shows the total costs for droop placements under various maximum K_{max} and $K_{sto,c}^M$ limits in the IEEE-118 bus test case. The costs are normalized by the current settings, i.e., $K_{max} = 165$ and $K_{sto,c}^M = 50$. It indicates that the total cost reduces under higher K_{max} and $K_{sto,c}^M$ limits. Therefore, large-scale centralized energy storage is more effective for frequency safety problems in low-inertia and large disturbances. Yet, land resources and operation safety are critical confinement factors for large energy storage stations. The load-side regulation resources are also significant for frequency stability. The essential primary regulation providers, such as EVs, base stations, computing centers, and distributed renewable energy, enlarges $K_{sto,c}^M$ and lower the total costs.

6.5. Discussions

6.5.1. Accuracy and benefits of the proposed control model
Complete AC model. The conventional unit models are a combination of a six-order generator, auto voltage regulator (AVR), power system stabilizer (PSS), governor and its control, and turbine module. The model is similar to the standard in PSD-ST [44]. All parameters in the
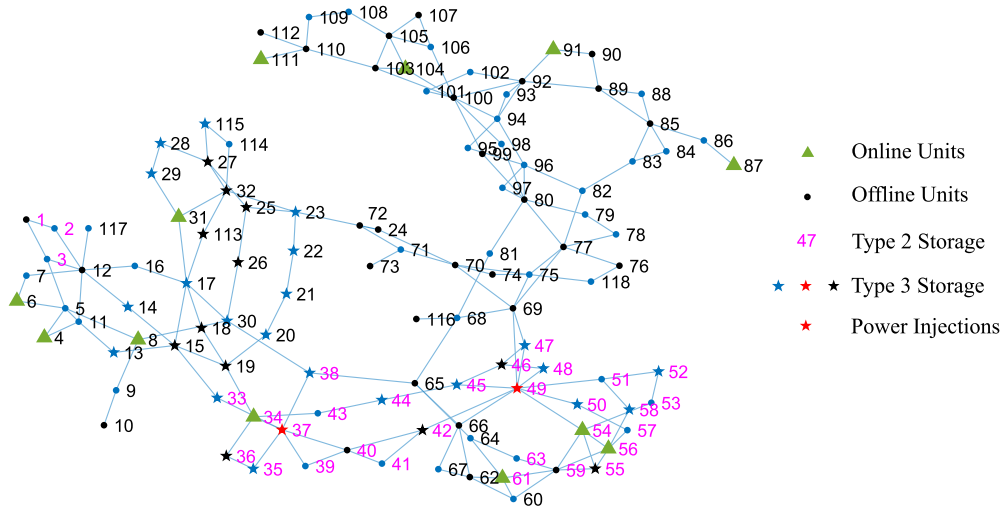
Fig. 17. Droop placements of IEEE 118-bus test case in operating mode 2 (the lowest online rate). Type 2 storage are on buses with magenta labels, while type 3 are on star-shaped buses. The red buses, 49 and 37 are cross-regional power injections. Units are online at green triangle-shaped buses. There are both Type 3 storage and power injections on bus 49 and 37.
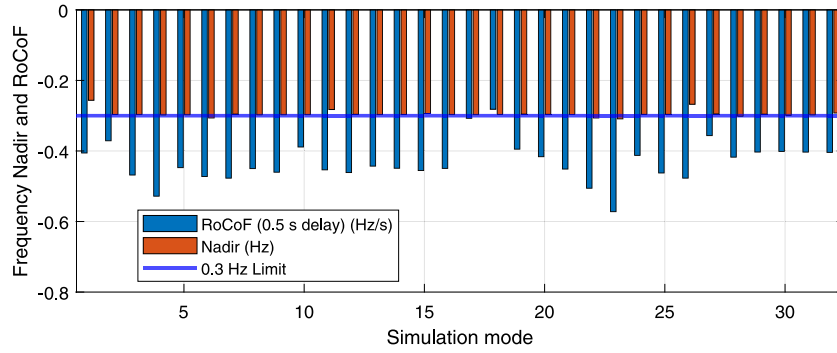

Fig. 18. Minimum frequency nadirs and RoCoF in IEEE 118-bus test case.
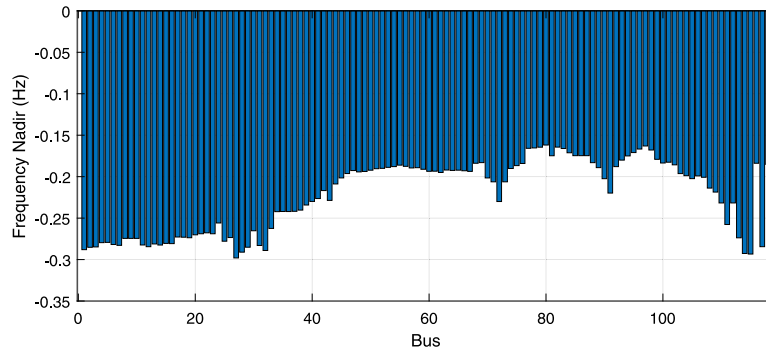

Fig. 19. Example of nodal frequency nadirs in IEEE 118-bus test case. Disturbances at bus 37, operating mode 15.

modules excluding those in Section 6.1 are from practical units in China Eastern Power Grids.

All power electronics operate in grid-following modes. The energy storage provides primary regulations responding to the frequency at PCC points through current controls.

The AC circuit formula Eq. (25) connects the voltage (V^{xy}) and current (I^{xy}) vectors among generators (mark as $\mathcal{G}$) and loads (including power electronics, mark as $\mathcal{L}$). The generators connect to the power grids through transformers. We apply ZIP and power-frequency-response models to power loads.

$$\begin{bmatrix} I_{\mathcal{G}}^{xy} \\ I_{\mathcal{L}}^{xy} \end{bmatrix} = \begin{bmatrix} Y_{\mathcal{G},\mathcal{G}} & Y_{\mathcal{G},\mathcal{L}} \\ Y_{\mathcal{L},\mathcal{G}} & Y_{\mathcal{L},\mathcal{L}} \end{bmatrix} \begin{bmatrix} V_{\mathcal{G}}^{xy} \\ V_{\mathcal{L}}^{xy} \end{bmatrix}. \tag{25}$$

Simulation results comparisons. We simulate and compare the frequency nadirs and responses after the disturbance in Fig. 19 with the complete AC and our proposed model.

Figs. 21 and 22 show the nodal frequency response curves in AC and the proposed models. The trends of nodal frequency curves are similar 0 ~ 2 seconds after disturbances. The nodal frequency nadirs are close in both two models. However, the internal oscillation tends to flatten faster in the complete AC model than in the proposed one. The power system stabilizer (PSS) systems provide additional damping through voltage controls.

Furthermore, Fig. 23 to 24 shows the nodal frequency nadirs using the AC and the proposed model at different buses. The frequency nadirs
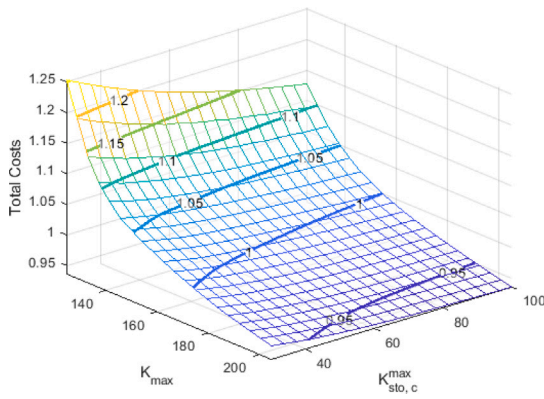
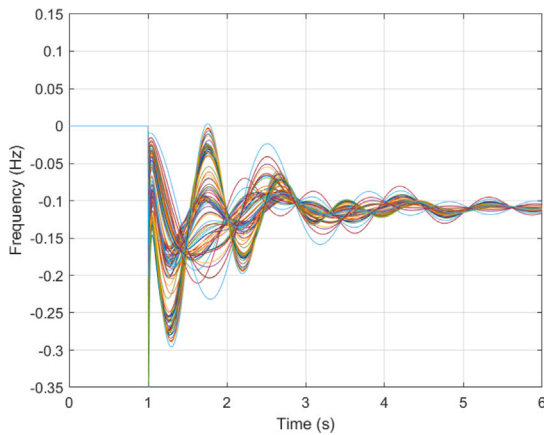**Fig. 20.** Economic costs under various maximum droop settings.

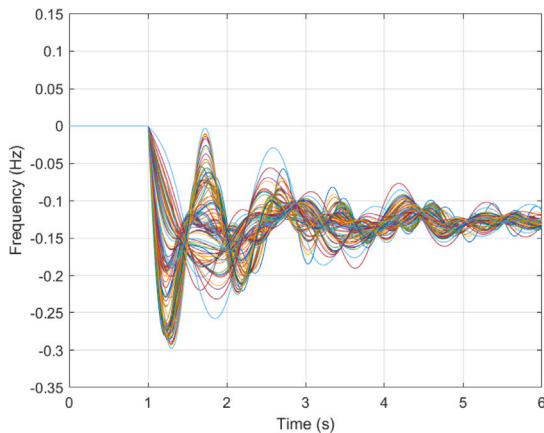**Fig. 21.** Frequency responses with the complete AC model. Mode 15, Disturbance 37.

Fig. 22. Frequency responses with the proposed model. Mode 15, Disturbance 37.

Fig. 23. Nodal frequency nadirs using the AC and the proposed model. Mode 15, Disturbance 49.

Fig. 24. Nodal frequency nadirs using the AC and the proposed model. Mode 15, Disturbance 37.

Table 3

Nodal frequency differences using the AC and the proposed model at mode 15.

Mode	Disturbance	Minimum nadir gap (Hz)	Mean absolute error (Hz)
15	49	0.0103	0.0155
15	37	0.0022	0.0148

Benefits of the proposed model. First, the proposed model does not require reactive power balancing when initializing the simulations. In the complete AC model, we must calculate ACOPF for the initial parameters, such as voltage magnitudes and angles. The convergence and computational efficiency of the ACOPF algorithm are still problems that need to be studied.

Second, the proposed model has a faster simulation speed. It takes around 0.1 s for the proposed model and 0.5 s for the complete AC model per simulation. Also, the proposed model is pure ODE. Thus, there is fewer numerical problem in the simulation.

6.5.2. The sampling strategy for rule extractions

The ideal sample sets should satisfy the following two conditions: First, the probability distributions of the sample data in each mode should be similar. As a result, the extracted rules are common to each mode. Second, the optimal droop placement results should be within the intersection among each mode's sampling data. In this case, the extracted rules would be effective for the optimization problem.

As for small-scale power systems, the sampling data can traverse the majority of droop placement plans. Thus, the rules extracted from

using AC models would be higher than the proposed models for several buses. It is because the conventional units' PSS systems provide extra damping and offset the frequency/angle oscillations as time passes. Also, the primary regulations from energy storage would lift up the nodal frequency nadirs [11].

Table 3 shows the statistic numbers on nodal frequency differences using the AC and the proposed model. The minimum nodal frequency nadirs gaps, and the mean absolute error (MAE) are within 0.02 Hz. The proposed method is relatively accurate compared with the AC model.
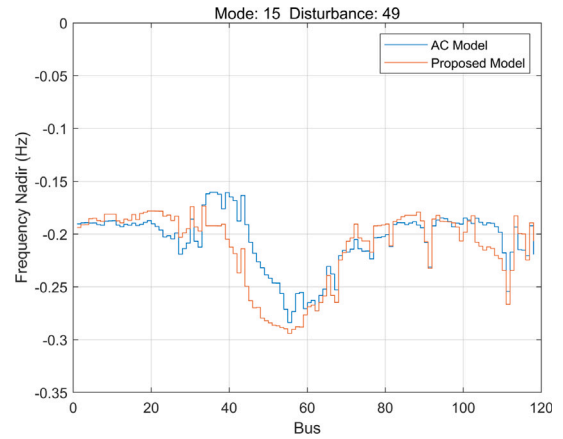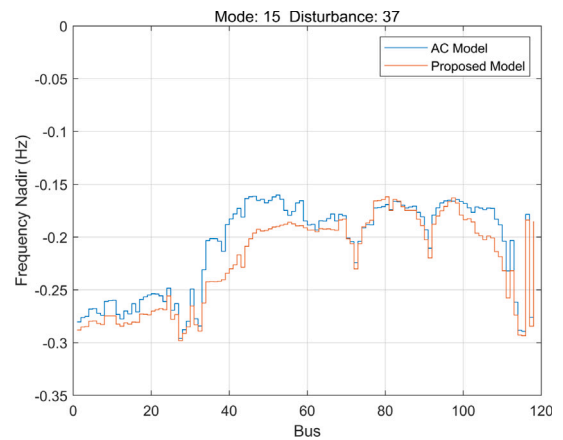
samplings are effective. When the nodal frequency response characteristics among different modes are similar (like the IEEE 39-bus case), the extracted rules can also be reliable. It is because the sampling spaces among modes are pretty similar. Besides, large amounts of existing (type 1) energy storage can narrow the solution spaces for droop placements (like the IEEE 118-bus case). The optimal solution may fall within the intersection of each mode's sampling dataset, which satisfies the requirements above. However, the sampling sets are nearly zero-measure for larger power systems compared with possible droop placement plans. The sampling sets could conflict with the conditions above and reduce the generalization performances of extracted rules. There are two strategies to enhance the sampling and rule extraction effectiveness.

Strategy 1. First, we may use the same initial sampling datasets for multiple modes. Then, we can randomly select part of additional samples from other modes and combine them with the current mode as the overall sampling set. In this way, the samples of a mode contain information from itself and others. The extracted rules and the optimal results would be reliable.

Strategy 2. It is possible that the verification results exceed the set frequency nadir limits (see Section 5.3). In this case, we could make new samplings and rule extractions near the current droop placement solution for bad-performance modes. If the optimal droop coefficients are sparse among buses, we can make only samplings on the buses with non-zero droops. Then, we solve the new optimization problem and verify the results. We may repeat the steps multiple times until the solution passes the verification. The frequency nadir problems are usually with good localized generalization. Thus, the number of samples in each step could be fewer than in Section 4.

The two strategies enhance the method's adaptability to general droop placement problems.

6.5.3. Applications to larger systems

The energy storage is placed close to the disturbance points and the neighborhood of the conventional unit, consistent with engineering experiences. The processes of rule extraction and optimization are less time-consuming. Yet, sampling data for large-scale power systems might take a lot of time. For example, a province-level power system may have around 1000 buses and hundreds of conventional units. There are several tips for energy storage placements in large systems.

1. Make sampling on the selected buses instead of the whole buses. The proportion of nodes suitable for installing energy storage is limited due to geographical limitations and other practical reasons.
2. Merge low voltage-level buses. The frequency oscillation characteristics among nodes absent of neighbor conventional units are almost identical. Buses can be aggregated by analysis or data-driven methods.
3. Make the best of parallel computing. Multi-core parallel computing effectively improves the sampling efficiency.
4. Establish rule databases for typical operating modes. It avoids repeated calculation and rule extractions for daily operations.

6.5.4. Prepare for new disturbance points

We should redo the simulations and rule extractions when new large-capacity HVDC systems are deployed in the power system. The original rules are still valid, and no additional changes are required for the original HVDC systems. We should put both original and new rules into the final optimization model for proper droop placement plans. Also, we should remove the corresponding rules when a HVDC system stops service permanently.

We assume the disturbances from HVDC failures are much more serious and frequent than others, such as unit trips. The assumption is based on the facts in Chinese power systems. China is planning and

running over twenty ±800 kV and ±1100 kV UHVDC systems. Each UHVDC carries 8–10 GW power across the country and may cause 4–5 GW imbalances after mono-polar blocking faults. By contrast, the maximum power outputs of conventional units are below 1 GW. Their daily power outputs would be much less than 1 GW due to high-renewable penetrations. Therefore, it is not necessary to consider the conventional unit disturbances.

6.5.5. Profitability to provide primary regulation services

Energy storage investment and profitability are important issues in the electricity markets. The economic benefit of energy storage is closely related to policies and market rules. Currently, energy storage makes profits through price compensations in ancillary service markets.

In low-inertia power systems, the primary regulation from energy storage critically influences the systems' operation modes. The prices of energy storage compensation can be determined (or as an important reference) by the shadow prices of energy storage constraints. For example, the maximum droop constraint, e.g., $K_{sto} \leq K_{sto}^{max}$, in frequency-constrained economic dispatch (FCED) problems may have different shadow prices over a day [49]. The strategy reflects the energy storage's practical contribution to frequency stability. Also, it might increase the profits for storage operators.

7. Conclusions and future works

The high-penetration renewable energy and cross-regional power injections increase the risks on power system frequency. Also, the large disturbances and the power system's heterogeneous characteristics make nodal frequency different on each bus. The effectiveness of energy storage's primary regulations differs on various buses. Thus, we use frequency divider theories to take the nodal frequencies into the frequency response model. First, we make massive simulations on different combinations of energy storage droop coefficients and apply ASVMTREE for rule extractions. Then, we build the optimization model based on the rules and make tests on modified IEEE 39- and 118-bus test cases. The results indicate the method's high accuracy and generality for droop coefficient placement problems in energy storage.

We summarize the contribution of the paper to the industry. First, we consider the nodal frequency response models instead of COI ones and reveal the differences in buses after large disturbances. Second, we use non-linear industry-level unit models instead of simplified ones. They are more suitable for representing the latest power plants built in the 21st century. Most previous studies did not consider secondary reheat thermal and hydro-units, which are common in modern power systems. Third, we have applied the method to large systems, such as IEEE 118-bus models. Finally, the data-driven method has good versatility. It is suitable for new generator models and auxiliary facilities, such as PSS and excitation systems.

The paper's main conclusions are: (1) It is necessary to take the power grids and local frequency into the response model, especially for large systems. (2) The rules extracted by ASVMTREE from simulations are accurate and effective for droop coefficient placements. (3) Type 2 energy storage (long-term deployed ones) is usually placed near the disturbances, and frequency nadirs are relatively low at those buses compared with COI ones. (4) Type 3 energy storage (movable ones) is deployed around the closest units to the disturbances as a supplementary.

We may take the grid-forming power electronics into swing and frequency divider models. Besides, energy storage can provide virtual inertia responses in future studies. We are going to apply the method to practical power system cases. There might be thousands of buses, hundred units, massive operating modes, and several possible disturbances in the system.
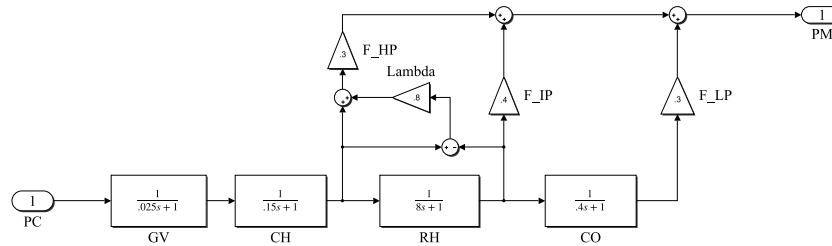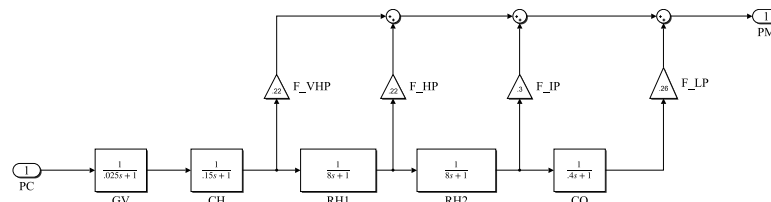
Fig. 25. Model of primary reheat generator.

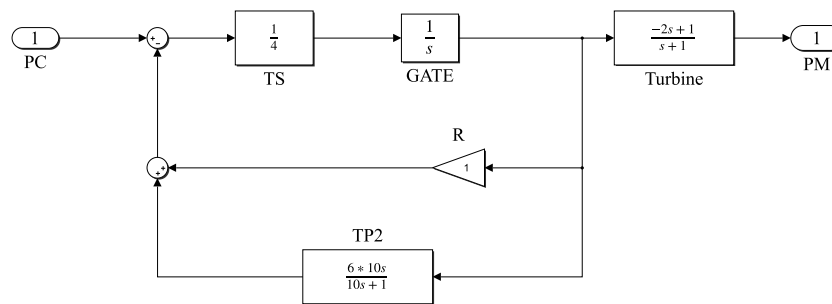**Fig. 26.** Model of secondary reheat generator.

Fig. 27. Model of hydro turbines.

CRediT authorship contribution statement

Jiawei Zhang: Writing – review & editing, Writing – original draft, Methodology, Investigation, Formal analysis, Conceptualization. **Jiaxin Wang:** Writing – review & editing, Validation, Investigation. **Ning Zhang:** Writing – review & editing, Supervision, Project administration, Investigation, Funding acquisition. **Peng Wang:** Funding acquisition. **Yating Wang:** Funding acquisition. **Chen Fang:** Funding acquisition.

Declaration of competing interest

The authors declare the following financial interests/personal relationships which may be considered as potential competing interests: Ning Zhang reports financial support was provided by National Key Research and Development Program of China.

Data availability

The authors do not have permission to share data.

Acknowledgments

Appendix

Control models of primary reheat (TB), secondary reheat (TC), hydro generators are shown in Fig. 25, 26 and 27. Gas turbines uses inertia links with $T_G = 1.2$ seconds, i.e., $G_{TG}(s) = \frac{1}{1.2s+1}$. These models are used in professional simulation software PSD-ST. It is maintained by China Electric Power Research Institute [44].

References

[1] Hou Q, Du E, Zhang N, Kang C. Impact of high renewable penetration on the power system operation mode: A data-driven approach. IEEE Trans Power Syst 2020;35(1):731–41.

[2] Kalair A, Abas N, Khan N. Comparative study of HVAC and HVDC transmission systems. Renew Sustain Energy Rev 2016;59:1653–75, URL https://www.sciencedirect.com/science/article/pii/S1364032115016718.

[3] A New Energy Network: HVDC Development in China, URL http://cleanandsecuregrid.org/2017/01/02/a-new-energy-network-hvdc-development-in-china/.

[4] Gao H, Yuan H, Xin H, Huang L, Feng C. Nodal frequency performance of power networks. In: 2019 IEEE 8th international conference on advanced power system automation and protection. 2019, p. 1838–42.

[5] Poolla BK, Bolognani S, Dörfler F. Optimal placement of virtual inertia in power grids. IEEE Trans Automat Control 2017;62(12):6209–20.

[6] Ørum E, Kuivaniemi M, Laasonen M, Bruseth AI, Jansson EA, Danell A, et al. Future system inertia. ENTSOE, Brussels, Tech. Rep, 2015, p. 1–58.

[7] Fradley J, Preece R, Barnes M. The influence of network factors on frequency stability. IEEE Trans Power Syst 2020;35(4):2826–34.

[8] Ma N, Wang D. Extracting spatial-temporal characteristics of frequency dynamic in large-scale power grids. IEEE Trans Power Syst 2019;34(4):2654–62.

[9] Milano F, Ortega A. Frequency divider. IEEE Trans Power Syst 2017;32(2):1493–501.

[10] Milano F, Manjavacas ÁO. Frequency Variations in power systems: modeling, state estimation, and control. John Wiley & Sons; 2020.

[11] Milano F, Ortega Á. A method for evaluating frequency regulation in an electrical grid – part I: Theory. IEEE Trans Power Syst 2021;36(1):183–93.

[12] Tan B, Zhao J, Duan N, Maldonado DA, Zhang Y, Zhang H, et al. Distributed frequency divider for power system bus frequency online estimation considering virtual inertia from DFIGs. IEEE J Emerg Sel Top Circuits Syst 2022;12(1):161–71.

[13] Farahani A, Abolmasoumi AH, Bayat M, Mili L. A fast outlier-robust fusion estimator for local bus frequency estimation in power systems. In: 2020 10th smart grid conference. 2020, p. 1–6.

[14] Zhao J, Mili L, Milano F. Robust frequency divider for power system online monitoring and control. IEEE Trans Power Syst 2018;33(4):4414–23.

[15] Milano F, Manjavacas AO. Frequency-dependent model for transient stability analysis. IEEE Trans Power Syst 2019;34(1):806–9.

[16] Badesa L, Teng F, Strbac G. Conditions for regional frequency stability in power system scheduling—Part I: Theory. IEEE Trans Power Syst 2021;36(6):5558–66.

[17] Calero F, Canizares CA, Bhattacharya K, Anierobi C, Calero I, de Souza MFZ, et al. A review of modeling and applications of energy storage systems in power grids. Proc IEEE 2022;1–26, , URL https://ieeexplore.ieee.org/document/9743285/.

[18] Zhang J, Wang P, Zhang N. Frequency regulation from distributed energy resource using cloud-edge collaborations under wireless environments. IEEE Trans Smart Grid 2021;1.

[19] Greenwood D, Lim K, Patsios C, Lyons P, Lim Y, Taylor P. Frequency response services designed for energy storage. Appl Energy 2017;203:115–27, URL https://www.sciencedirect.com/science/article/pii/S0306261917307729.

[20] Calero F, Cañizares CA, Bhattacharya K, Anierobi C, Calero I, de Souza MFZ, et al. A review of modeling and applications of energy storage systems in power grids. Proc IEEE 2023;111(7):806–31.

[21] Cheng M, Sami SS, Wu J. Benefits of using virtual energy storage system for power system frequency response. Appl Energy 2017;194:376–85, URL https://www.sciencedirect.com/science/article/pii/S0306261916308881.

[22] Feng C, Chen Q, Wang Y, Kong P-Y, Gao H, Chen S. Provision of contingency frequency services for virtual power plants with aggregated models. IEEE Trans Smart Grid 2023;14(4):2798–811.

[23] Feng C, Chen Q, Wang Y, Ma J, Wang X. Frequency regulation service provision for virtual power plants through 5G RAN slicing. IEEE Trans Smart Grid 2022;13(6):4943–56.

[24] Zhong W, Tzounas G, Milano F. Real-time estimation of VPP equivalent inertia and fast frequency control. In: 2022 IEEE power and energy society general meeting. 2022, p. 1–5.

[25] Oshnoei A, Kheradmandi M, Blaabjerg F, Hatziargyriou ND, Muyeen S, Anvari-Moghaddam A. Coordinated control scheme for provision of frequency regulation service by virtual power plants. Appl Energy 2022;325:119734, URL https://www.sciencedirect.com/science/article/pii/S0306261922010236.

[26] Xu G, Zhu C, Bi T, Xue A, Hu J. Optimal frequency controller parameters of wind turbines participating system frequency control. In: 2018 IEEE power and energy society general meeting. 2018, p. 1–5.

[27] Huang J, Yang Z, Yu J, Xiong L, Xu Y. Frequency dynamics-constrained parameter design for fast frequency controller of wind turbine. IEEE Trans Sustain Energy 2022;13(1):31–43.

[28] Cui W, Jiang Y, Zhang B. Reinforcement learning for optimal primary frequency control: A Lyapunov approach. IEEE Trans Power Syst 2023;38(2):1676–88.

[29] Jiang Y, Cui W, Zhang B, Cortés J. Stable reinforcement learning for optimal frequency control: A distributed averaging-based integral approach. IEEE Open J Control Syst 2022;1:194–209.

[30] Cai G, Zhou S, Liu C, Zhang Y, Guo S, Cao Z. Hierarchical under frequency load shedding scheme for inter-connected power systems. Protect Control Modern Power Syst 2023;8(1):34.

[31] Zhang C, Liu L, Cheng H, Liu D, Zhang J, Li G. Frequency-constrained co-planning of generation and energy storage with high-penetration renewable energy. J Mod Power Syst Clean Energy 2021;9(4):760–75.

[32] Knap V, Chaudhary SK, Stroe D-I, Swierczynski M, Craciun B-I, Teodorescu R. Sizing of an energy storage system for grid inertial response and primary frequency reserve. IEEE Trans Power Syst 2016;31(5):3447–56.

[33] Nguyen N, Bera A, Mitra J. Energy storage to improve reliability of wind integrated systems under frequency security constraint. IEEE Trans Ind Appl 2018;54(5):4039–47.

[34] Wen Y, Li W, Huang G, Liu X. Frequency dynamics constrained unit commitment with battery energy storage. IEEE Trans Power Syst 2016;31(6):5115–25.

[35] Poolla BK, Groß D, Dörfler F. Placement and implementation of grid-forming and grid-following virtual inertia and fast frequency response. IEEE Trans Power Syst 2019;34(4):3035–46.

[36] Ademola-Idowu A, Zhang B. Frequency stability using MPC-based inverter power control in low-inertia power systems. IEEE Trans Power Syst 2021;36(2):1628–37.

[37] Zhang Y, Cui H, Liu J, Qiu F, Hong T, Yao R, et al. Encoding frequency constraints in preventive unit commitment using deep Learning With Region-of-interest active sampling. IEEE Trans Power Syst 2022;37(3):1942–55.

[38] Lagos DT, Hatziargyriou ND. Data-driven frequency dynamic unit commitment for island systems with high RES penetration. IEEE Trans Power Syst 2021;36(5):4699–711.

[39] Hou Q, Zhang N, Kirschen DS, Du E, Cheng Y, Kang C. Sparse oblique decision tree for power system security rules extraction and embedding. IEEE Trans Power Syst 2021;36(2):1605–15.

[40] Sun M, Konstantelos I, Strbac G. A deep learning-based feature extraction framework for system security assessment. IEEE Trans Smart Grid 2019;10(5):5007–20.

[41] Zhang Y, Chen C, Liu G, Hong T, Qiu F. Approximating trajectory constraints with machine learning – microgrid islanding with frequency constraints. IEEE Trans Power Syst 2021;36(2):1239–49.

[42] Zhang J, Jia H, Zhang N. Alternate support vector machine decision trees for power systems rule extractions. IEEE Trans Power Syst 2023;38(1):980–3.

[43] Jin Z, Wang X. A DQ-frame asymmetrical virtual impedance control for enhancing transient stability of grid-forming inverters. IEEE Trans Power Electron 2022;37(4):4535–44.

[44] PSD-ST transient stability program user manual. 5th ed.. China Electric Power Research Institute; 2015.

[45] Zhang Z, Du E, Teng F, Zhang N, Kang C. Modeling frequency dynamics in unit commitment with a high share of renewable energy. IEEE Trans Power Syst 2020-11;35(6):4383–95.

[46] Zhang L, Suganthan PN. Oblique decision tree ensemble via multisurface proximal support vector machine. IEEE Trans Cybern 2015;45(10):2165–76.

[47] China Power Engineering Consulting Group Co, Ltd. Power enginnering design manual: power system planning and design. China Electric Power Press; 2019.

[48] Nedd M, Browell J, Bell K, Booth C. Containing a credible loss to within frequency stability limits in a low-inertia GB power system. IEEE Trans Ind Appl 2020;56(2):1031–9.

[49] Li K, Guo H, Fang X, Liu S, Teng F, Chen Q. Market mechanism design of inertia and primary frequency response with consideration of energy market. IEEE Trans Power Syst 2022;1–13.